

FORTGESCHRITTENEN PRAKTIKUM II

Z0 Resonance

26.03.2016

Benjamin Winkelmann
Peter Spalthoff

Tutor: Christian Lüdtke

Abstract

The Z^0 Boson is the neutral partner of the W^\pm carrier particle of the weak interaction in the Standard Model. At CERN, the Large Electron-Positron Collider (LEP) collided electrons and positrons with center-of-mass energies around 91.2 GeV, thereby resonantly creating the short-lived Z^0 . In this protocol, data collected by the "Omni-Purpose Apparatus for LEP" (OPAL) is analyzed to test fundamental features of the Standard Model and specifically of the electroweak interaction.

By extracting the cross sections of several Z^0 decays for different center-of-mass energies and fitting the theoretically expected curve to this data, the Z^0 mass and the total decay width were determined to be $M_Z = (91.188 \pm 0.008)$ GeV and $\Gamma_Z = (2.516 \pm 0.017)$ GeV.

The number of neutrino generations was then calculated to be $n_\nu = 2.93 \pm 0.26$, confirming with reasonable certainty the existence of three neutrino generations.

Contents

List of Figures	III
List of Tables	IV
1. Physical Principles	1
1.1. Standard Model	1
1.2. Electroweak force and Weinberg Angle	1
1.3. Cross Section and decay width	2
1.4. e^-e^+ -interactions	3
1.5. Radiation correction	5
1.6. Forwards-backwards Asymmetry	6
2. LEP and the OPAL detector	7
2.1. LEP	7
2.2. OPAL	7
3. Data analysis	10
3.1. Event signatures	10
3.2. Selection of cuts	14
3.3. Two-photon events	21
3.4. Purity and the efficiency matrix	21
3.5. Calculation of the inverse efficiency matrix	23
3.6. Separation of s- and t-channel	24
3.7. Cross sections and the mass of Z^0	25
3.8. Decay widths and the neutrino generations	27
3.9. Forward-backward asymmetry	29

4. Conclusion	31
5. References	32
A. Calculation of decay widths and cross sections at resonance	33
A.1. Decay widths	33
A.2. Cross sections at resonance peak	34
B. Figures	35
B.1. Cross section fit graphs	35

List of Figures

1.1.	Standard Model	1
1.2.	Feynman diagramm: $e^-e^+ \rightarrow f\bar{f}$ (s-channel)	3
1.3.	Cross section as a function of CMS	4
1.4.	Feynman diagram: Bhabha scattering	4
1.5.	Feynman diagram: initial and final state radiation	5
1.6.	Feynman diagrams: virtual radiation	5
1.7.	Feynman daigrams: gluon radiation	6
2.1.	Bird's eye view LEP	7
2.2.	Opal schematic build up	8
3.1.	OPAL cross secion electron event	10
3.2.	OPAL cross section muon event	11
3.3.	OPAL cross section tauon event	12
3.4.	OPAL cross section quark event	13
3.5.	Ncharged in simulation data	15
3.6.	Pcharged in simulation data	16
3.7.	E_Ecal in simulations	17
3.8.	E_Hcal in simulation data	18
3.9.	Cos_theta in simulation data	19
3.10.	Cos_thru in simulation data	20
3.11.	Two-photon Feynman-graph	21
3.12.	s-t-channel separation $\sqrt{s} \approx 92 \text{ GeV}$ GeV	25
3.13.	Cross sections for muon cut	27
B.1.	Cross sections for electron cut	35
B.2.	Cross sections for tauon cut	36
B.3.	Cross sections for quark cut	36

List of Tables

3.1. Table of cuts	20
3.2. Efficiency matrix	22
3.3. Efficiency error matrix	22
3.4. Purity of the cuts	23
3.5. Inverse efficiency matrix	23
3.6. Inverse efficiency error matrix	24
3.7. Table of luminosities	26
3.8. Breit-Wigner fit results: M_{Z^0}	27
3.9. Breit-Wigner fit results: Decay widths	28
3.10. A_fb and the Weinberg angle	29
A.1. Partial decay widths	34
A.2. Summarized decay widths	34
A.3. $e^+e^- \rightarrow f\bar{f}$ cross sections	35
B.1. Decay widths not assumint universality	37

1. Physical Principles

1.1. Standard Model

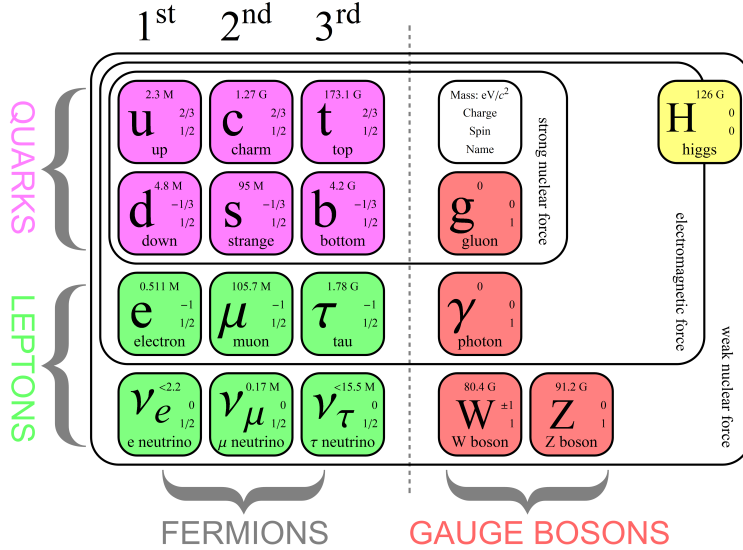


Figure 1.1: Fundamental particles in the Standard Model. [7]

Figure 1.1 gives an overview of the fundamental particles in the Standard Model. Quarks and Leptons obey the Pauli exclusion principle and are therefore fermions. Each of those also has a corresponding antiparticle with the same mass but opposite charge. Fundamental interactions are mediated by the Gauge Bosons, namely two particles interact with each other by exchanging said bosons. The original theory stated that fermions and bosons are massless, they gain mass via the Higgs-Kibble mechanism which implies the existence of another particle, the Higgs Boson [4].

1.2. Electroweak force and Weinberg Angle

In 1967 Glashow, Salam and Weinberg were able to formulate a theory that unified the electromagnetic and weak force. In this model, the electroweak interaction is mediated by the four Bosons W^1 , W^2 , W^3 and B^0 . The Bosons of the Standard Model are then described as a linear combination of those Bosons; two charged states

$$|W^\pm\rangle = (1/\sqrt{2})(|W^1\rangle \mp i|W^2\rangle) \quad (1.1)$$

and the photon and Z^0 Boson as orthogonal neutral states [5]

$$\begin{aligned} |\gamma\rangle &= \cos(\theta_w)|B^0\rangle + \sin(\theta_w)|W^3\rangle \\ |Z^0\rangle &= -\sin(\theta_w)|B^0\rangle + \cos(\theta_w)|W^3\rangle \end{aligned} \quad (1.2)$$

The mixing angle θ_w is now commonly called *Weinberg angle*, although it was originally the *weak mixing angle*. Furthermore, it is related to the fine-structure constant α , the Fermi coupling constant G_F and the mass of the Z^0 Boson [4]:

$$\sin^2(\theta_w) \cdot \cos^2(\theta_w) = \frac{\pi\alpha}{\sqrt{2}G_FM_Z^2} \quad (1.3)$$

The mass of the W^\pm Bosons can be expressed as:

$$M_W = M_Z \cos(\theta_w) \quad (1.4)$$

In electroweak interaction, one distinguishes two forms of coupling, vector coupling (changes sign under parity transformation) and axial vector coupling (does not change sign under parity transformation). The coupling strengths for a fermion f with the third component of the weak isospin I_3^f and the charge Q_f is given by [4]:

$$\begin{aligned} g_V^f &= I_3^f - 2Q_f \sin^2(\theta_w) \\ g_A^f &= I_3^f \end{aligned} \quad (1.5)$$

1.3. Cross Section and decay width

The cross section σ is a measure for the probability or rate of a reaction during a collision of two particles. In this experiment, it is related to the Luminosity L of the electron beam and the total number of reactions N :

$$\sigma = \frac{N}{\int L dt} \quad (1.6)$$

In those collisions new particles can be created that in turn may decay with a mean life time T . Heisenberg's uncertainty principle relates the mean life with the (total) *decay width*:

$$\hbar = T \cdot \Gamma \quad (1.7)$$

Often, the particle can decay through different channels. The probability that a decay takes channel i is called the branching ratio BR_i . It can be described with the *partial* decay width Γ_i :

$$\Gamma = \sum_i \Gamma_i \quad (1.8)$$

The branching ratio is then:

$$BR_i = \frac{\Gamma_i}{\Gamma} \quad (1.9)$$

1.4. e^-e^+ -interactions

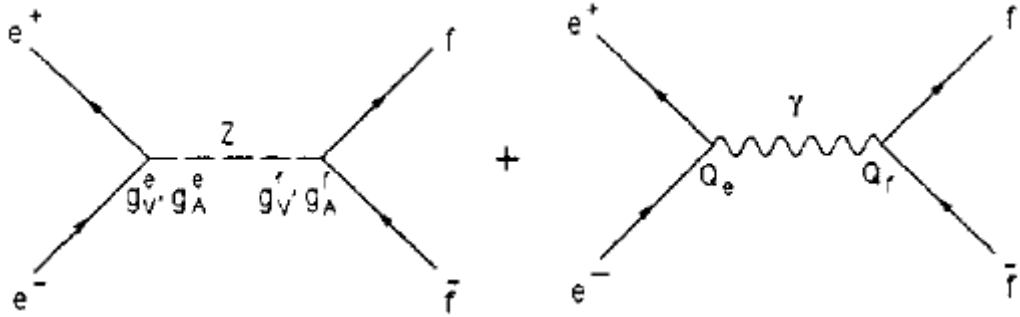


Figure 1.2: Feynman diagram of the $e^-e^+ \rightarrow f\bar{f}$ in first order, where f is an arbitrary fermion. [4]

The reaction of interest for this experiment is the $e^-e^+ \rightarrow f\bar{f}$ interaction. Figure 1.2 shows the s-channel: Electron and positron annihilate each other and a Z^0 Boson or a photon is produced, which in turn decay to a lepton or a quark and its corresponding antiparticle (except for the top quark, since the center-of-mass energy is less than the mass of two top quarks). The photon process is suppressed at energies close to the mass of the Z^0 boson[4].

The cross section for the $e^-e^+ \rightarrow f\bar{f}$ reaction is a function of the center-of-mass energy, which exhibits a peak at 91.187 GeV caused by the Z^0 resonance (s. fig 1.3).

Neglecting the fermion masses and at energies close to the resonance, this function can be described with a Breit-Wigner curve¹[4]:

$$\sigma_f(s) = \frac{12\pi}{M_Z^2} \frac{s\Gamma_e\Gamma_f}{(s - M_Z^2)^2 + s^2\Gamma_Z^2/M_Z^2} \quad (1.10)$$

Where \sqrt{s} is the center-of-mass energy, M_Z the Z_0 mass, Γ_Z the total decay width, Γ_e the partial decay width for electrons and Γ_f the partial decay width of the produced fermion.

¹For a table of theoretical decay widths and cross section and their calculation s. appendix

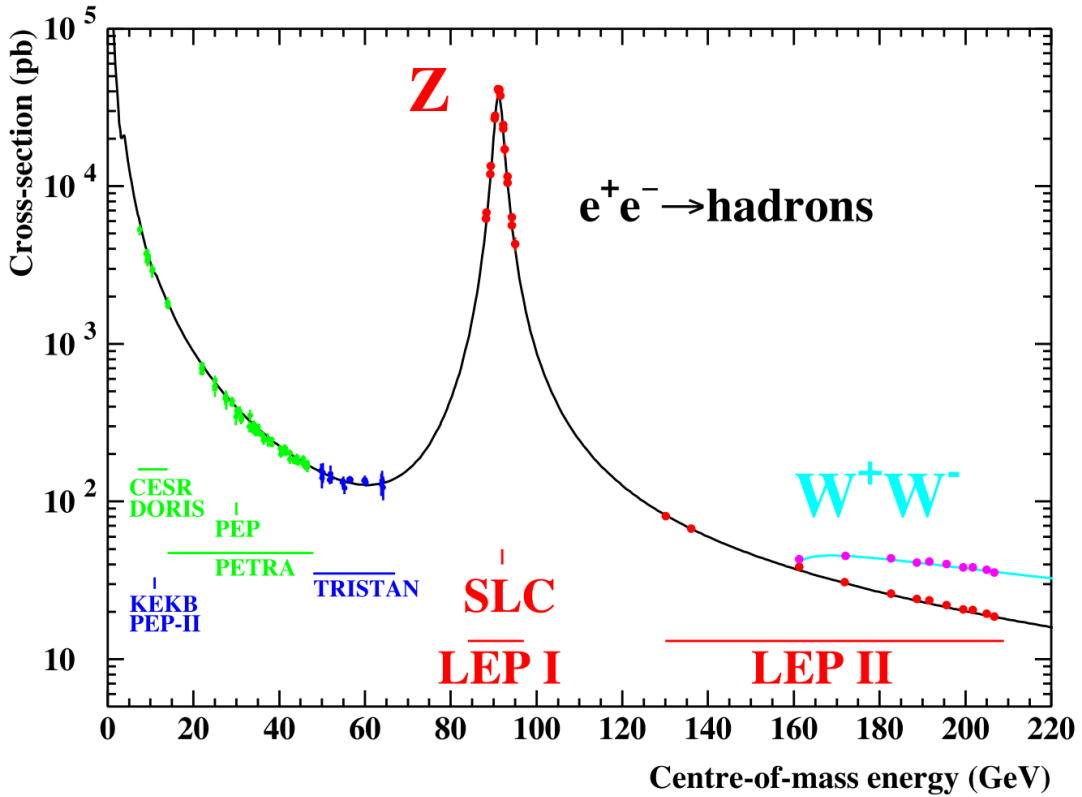


Figure 1.3: Cross section for the $e^+e^- \rightarrow q\bar{q}$ reaction as a function of the center-of-mass energy. The peak at 91.187 GeV is the Z^0 resonance peak. [6]

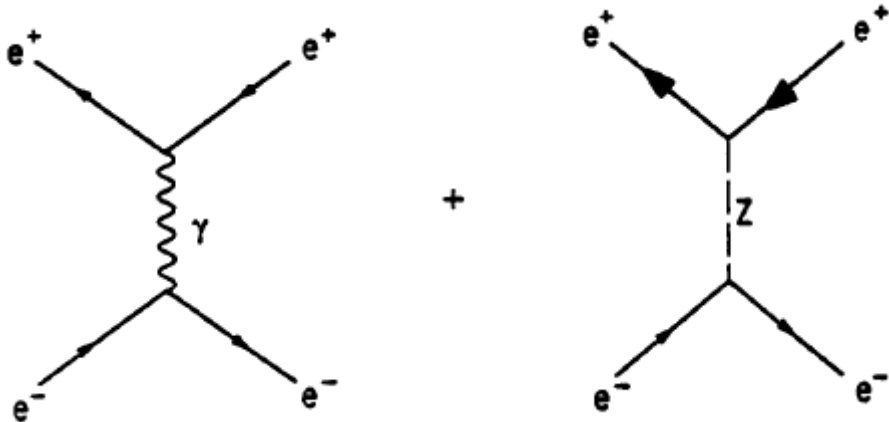


Figure 1.4: Feynman diagrams of the $e^-e^+ \rightarrow e^-e^+$ scattering (t-channel). [4]

Figure 1.4 shows the t-channel of the $e^-e^+ \rightarrow e^-e^+$ reaction. The partial cross sections for s- and t-channel differ in their dependency on the polar angle θ , which is the angle

between the positron beam direction and the created positive lepton [1]:

$$\frac{d\sigma_s}{d\Omega} \propto (1 + \cos^2(\theta)), \quad \frac{d\sigma_t}{d\Omega} t \propto (1 - \cos(\theta))^{-2} \quad (1.11)$$

1.5. Radiation correction

The Feynman diagrams in the previous chapter were only of first order. Neglecting higher orders (Born approximation) does not yield accurate predictions [4]. Three different corrections have to be made: The photonic, the non-photonic and the quantum chromodynamic (QCD) correction.

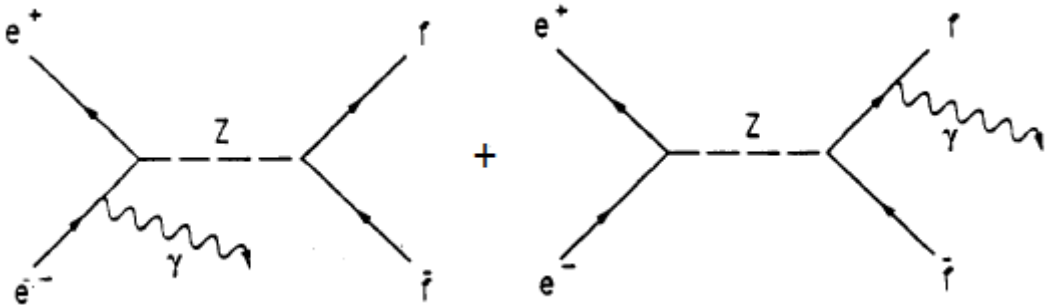


Figure 1.5: Feynman diagram for initial state (left) and final state radiation (right). [4]

During initial and final state radiation (see fig. 1.5), a photon is emitted. The energy this photon carries is not available for Z^0 production. Therefore, at center-of-mass energies $\sqrt{s} \leq M_Z$, this process decreases the cross section and for energies $\sqrt{s} > M_Z$ the cross section is increased.

Non photonic processes have the same final state as the first order process, but as seen in figure 1.6, the interaction is complicated by vertex loops. Those additional Feynman diagrams have to be accounted for in the cross section.

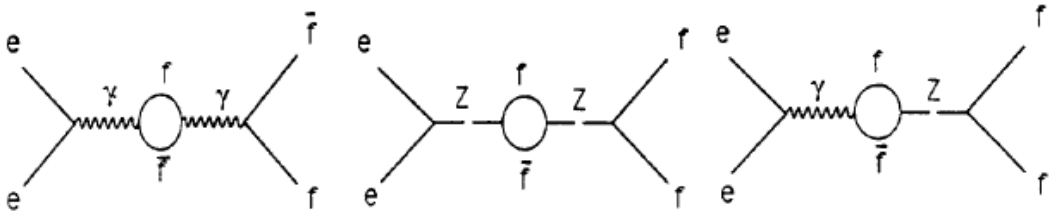


Figure 1.6: Feynman diagrams for virtual radiation correction. The final state is the same as in figure 1.2, but the path is complicated by vertex loops. [4]

If the produced fermions are quarks, an additional correction has to be made to account for gluon radiation (fig 1.7) of the strong interaction.

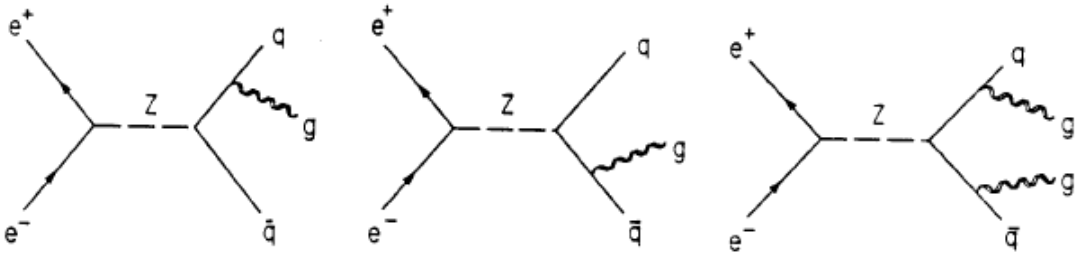


Figure 1.7: Feynman diagrams of gluon radiation. In contrast to leptons, quarks interact not only electroweak but also via the strong force and can radiate gluons. [4]

1.6. Forwards-backwards Asymmetry

The spherical coordinates introduced for equation 1.11 allow the definition of cross sections for the forward and backward hemisphere:

$$\sigma_f = \int_0^1 \frac{d\sigma}{dcos(\theta)} dcos(\theta) \quad \sigma_b = \int_{-1}^0 \frac{d\sigma}{dcos(\theta)} dcos(\theta) \quad (1.12)$$

The forwards backwards asymmetry is then defined as:

$$A_{fb} = \frac{\sigma_f - \sigma_b}{\sigma_f + \sigma_b} \quad (1.13)$$

At the resonance peak the difference in coupling strength for vector and axial vector coupling (s. eq.1.5) causes an asymmetry as defined above. For leptons it can be expressed as:

$$A_{fb}^{\ell,peak} \approx 3 \left(\frac{g_V^\ell}{g_A^\ell} \right)^2 = 3 \cdot (1 - 4sin^2(\theta_w)) \quad (1.14)$$

2. LEP and the OPAL detector

2.1. LEP



Figure 2.1: Bird's eye view of the Large Electron-Positron Collider at Cern in Geneva, Switzerland. Today, the large circular collider tunnel is used for the Large Hadron Collider (LHC). The smaller circle belonged to the Super Proton Synchrotron (SPS) experiment. [6]

The Large Electron-Positron Collider is storage ring with a diameter of 27 km. It accelerated 4 bunches of $4 \cdot 10^{11}$ electrons and positrons in opposite directions for about 20 hours. At four predetermined points (the positions of the detectors: Aleph, Delphi, L3 and OPAL) the beams collided about every $25\mu s$, but the reaction $e^+e^- \rightarrow f\bar{f}$ only occurred at a frequency of roughly 1Hz [4].

2.2. OPAL

The OPAL detector consists of several components arranged in a shell-like manner (see figure 2.2). Closest to the beam is the central tracking chamber (red), enabling tracking of charged particles. It is followed by the electromagnetic calorimeter (cyan), which is

used to determine the energy of positrons, electrons and photons. Next is the hadronic calorimeter (yellow), measuring the energy of hadrons passing through the electromagnetic calorimeter. The outermost shell are the muon detectors (blue), which, as the name suggests, are used to detect muons [9].

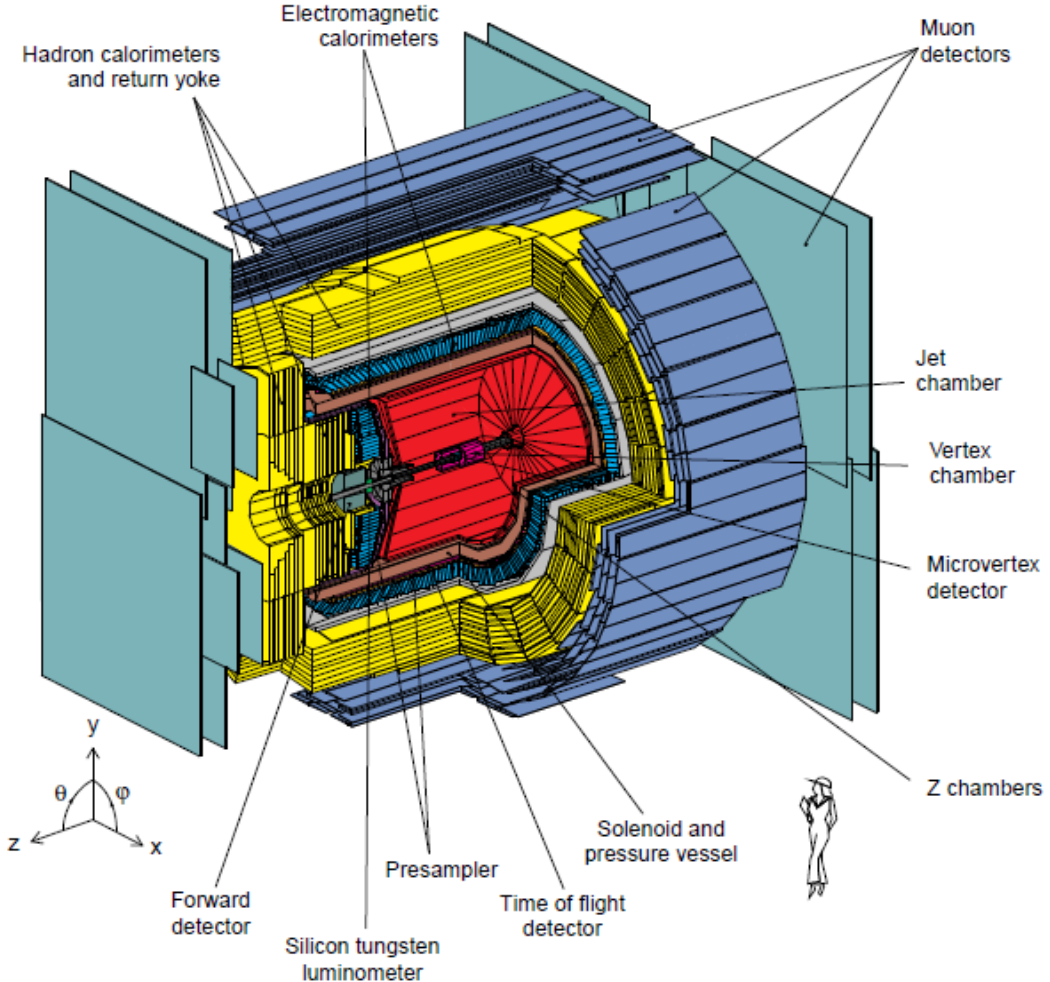


Figure 2.2: Schematic structure of the opal detector. The different types of detecting units are arranged in shells around the beam path. [9]

Tracking chamber: A charged particle passing through the detector ionizes atoms of the filling gas. The freed electrons (primary electrons) are accelerated towards anode wires spanned between two cathode plates and ionize more atoms, thus creating a shower of secondary electrons. Each of the anode wires can be read out separately. At constant drift velocities, the time difference between the passing of the (charged) particle and the

response of the wire is proportional to the distance of the track. One can determine the track by measuring those time differences. The chamber is additionally surrounded by a coil creating a magnetic field parallel to the e^+e^- -beam, thus forcing the charged particles on a circular trajectory. From the radius of this trajectory one can infer the particle's momentum [1].

Electromagnetic Calorimeter: OPAL's electromagnetic calorimeter is a total absorption calorimeter mostly made of lead-glass blocks [9]. High energy electrons and photons passing through the detector lose energy primarily due to bremsstrahlung (electron) and pair production (photon). The created secondary particles also lose energy this way, resulting in showers of particles, each generation with less energy. The shower ends when the energy of those particles is lower than the critical energy E_C at which the energy of electrons due to bremsstrahlung is equal to the loss due to ionization. The deposited energy is proportional to the energy of the original particle [4].

Hadronic Calorimeter: The principle is the same as above, but instead of bremsstrahlung and pair production, a different effect causes the showers.. A hadronic shower forms when a strongly interacting particle hits an absorber: in a series of inelastic collisions with the nuclei of the absorber, secondary hadrons are created, which also are scattered inelastically. The cascade stops once the particles have so little energy that they can be absorbed completely.

Muon detector: The Muon detector consists of 4 layers of muon chambers. They function like the tracking chamber but since all other charged particles are absorbed in the previous shells, only muons leave a track in this detector [4].

3. Data analysis

As no data was surveyed by the authors, there will be no chapter on the experimental procedure. Instead, the focus will be on the data analysis, for most of which the framework ROOT was used. Data was provided from two sources:

1. Monte Carlo simulations, separated by decay reaction.
2. Actual data from the OPAL detector at the LEP collider.

3.1. Event signatures

The four main types of events leave distinct signatures, which can be inspected in the detector cross sections. Examples are shown in figures 3.1 to 3.4.

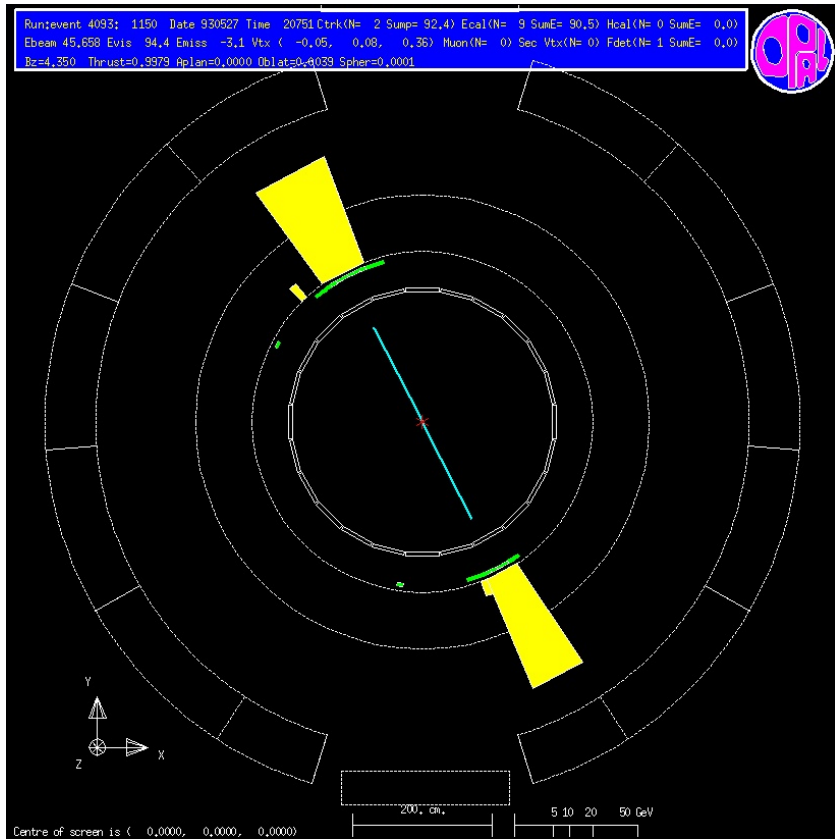


Figure 3.1: The OPAL cross section of an electron event. The energy deposition only being in the electromagnetic calorimeter clearly characterizes this event. [9]

Electron event: The two charged tracks in the drift chamber and the large depositions in the electromagnetic calorimeter (yellow bars) are characteristic for an electron event. Additional depositions in the electromagnetic calorimeter are due to bremsstrahlung.

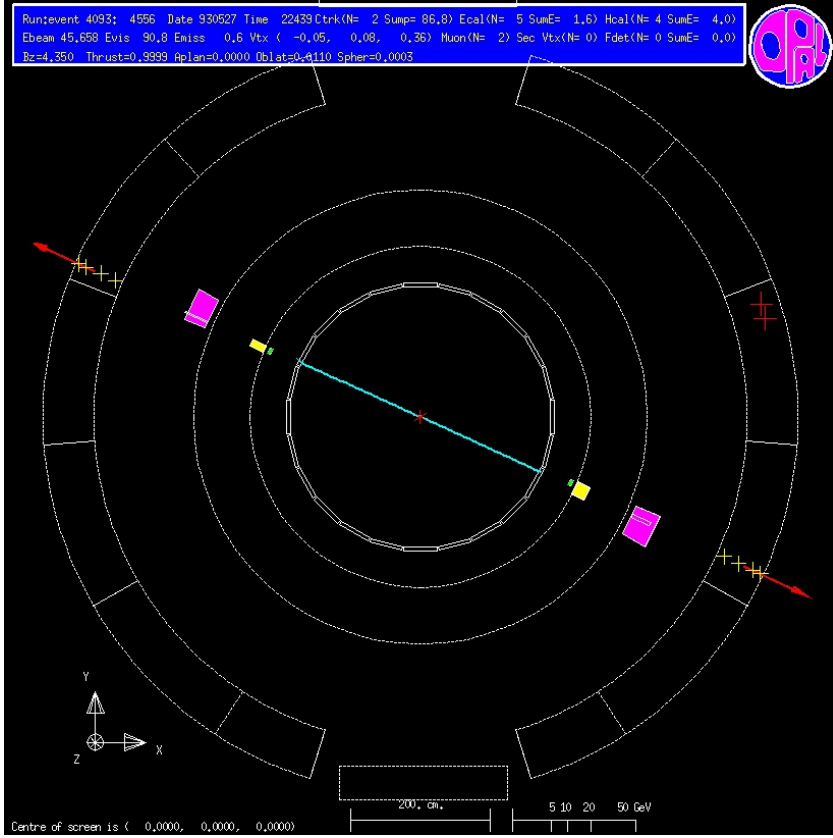


Figure 3.2: OPAL cross section of a muon event. The red arrows in the muon chambers (outermost ring) make muon events easy to spot. [9]

Muon event: Muons only interact very weakly with matter, which explains the low depositions in both the electromagnetic and hadronic calorimeters (purple bars). The muon chambers detect the exiting muons, which is depicted as red vectors pointing outward in figure 3.2.

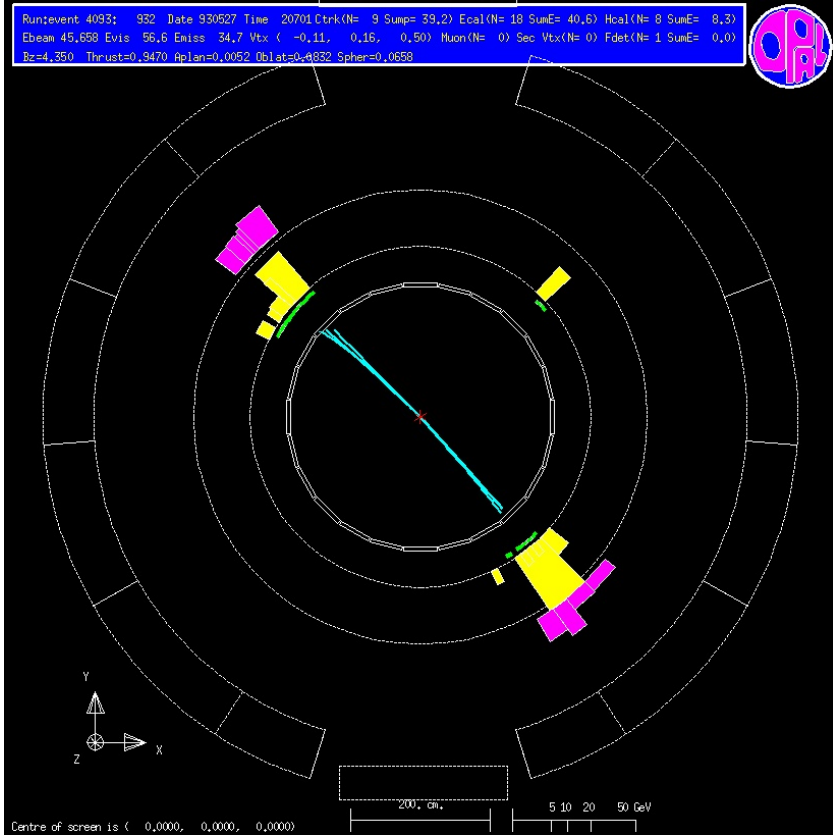


Figure 3.3: OPAL cross section of a tauon event. Tauon are very short lived and have in this case decayed to four charged pions. [9]

Tauon event: The short life span of tauons makes their signature more complex and diverse. In above figure, one tauon decayed to one charged pion while the other decayed to three charged pions. There are many other possibilities, in all of which undetected neutrinos or anti-neutrinos are also created. The tauon decays hadronically roughly 64.79% of the time and otherwise leptonically into a tau-neutrino, an electron or muon and the respective anti-neutrino [8].

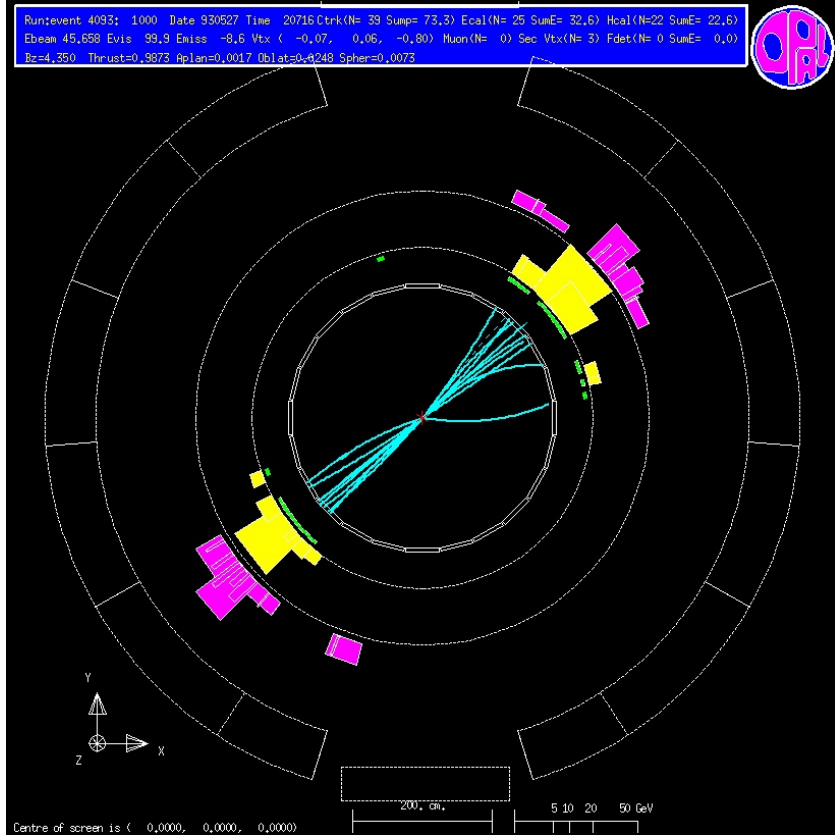


Figure 3.4: Opal cross section of a quark event. The particle jet and the large depositions in the hadronic calorimeter are characteristic for a quark decay. [9]

Quark event: These events are easily recognizable by the large number of charged particles, the so-called hadron jets. The energy is deposited in both electromagnetic and hadronic calorimeters. The number of tracks can be as high as 35.

3.2. Selection of cuts

In a first step, the data from the Monte Carlo simulations is plotted over adequate ranges in the following parameters:

- **NCHARGED:** The number of tracks visible in the drift chamber
- **PCHARGED:** Energy of particles that left a track in the drift chamber
- **E_ECAL:** Energy deposited in the electromagnetic calorimeter
- **E_HCAL:** Energy deposited in the hadronic calorimeter
- **COS_THET:** Angle θ between created the positive lepton and the incident positron beam
- **COS_THRU:** Angle between the thrust axis for hadronic events and the incident positron beam

These plots include the simulation events from decays to electrons, muons, tauons as well as quarks in similar amounts. These ratios are not a representation of the actual ratios as they would be expected in the real data, as the decay width of quarks is much greater than that of the three types of leptons.

To further improve comparability of the different data sets, all histograms were normed to an integral of 1. The resulting plots are shown in figures 3.5 to 3.10. Using these graphs, as well as the knowledge of the type of event, cuts are established which will later be used to separate the actual data, where there is no initial knowledge of the type of event.

Thus, for every type of educts, a cut is to be made with maximum possible efficiency in detecting the respective kind of event, as well as maximum purity, meaning that other events are falsely allotted as rarely as possible.

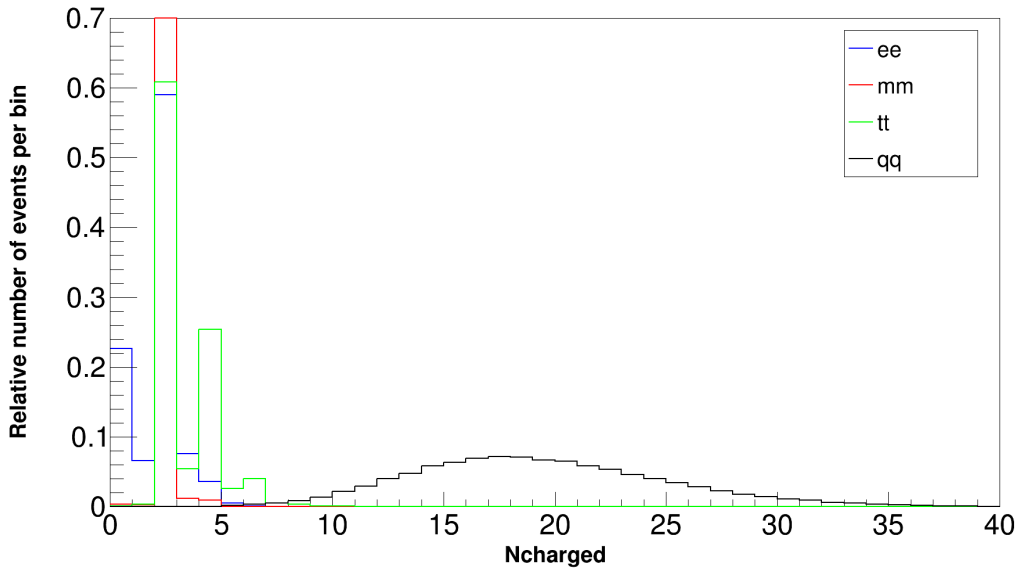


Figure 3.5: The number of charged tracks in the simulation data for the various decay events (color-coded). Almost all muon events leave two tracks. The peak is cut off to increase visibility of the other data.

3.2.1. Cuts in N_{charged}

Above figure suggests a good way to separate the data sets. In particular, all three lepton generations hardly ever leave more than 6 tracks, with muons hardly having anything but two tracks in the drift chamber. This suggests the following cuts:

- **Elektron cut:** $N_{\text{charged}} < 7$
- **Muon cut:** $N_{\text{charged}} = 2$
- **Tauon cut:** $N_{\text{charged}} < 7$
- **Quark cut:** $N_{\text{charged}} \geq 8$

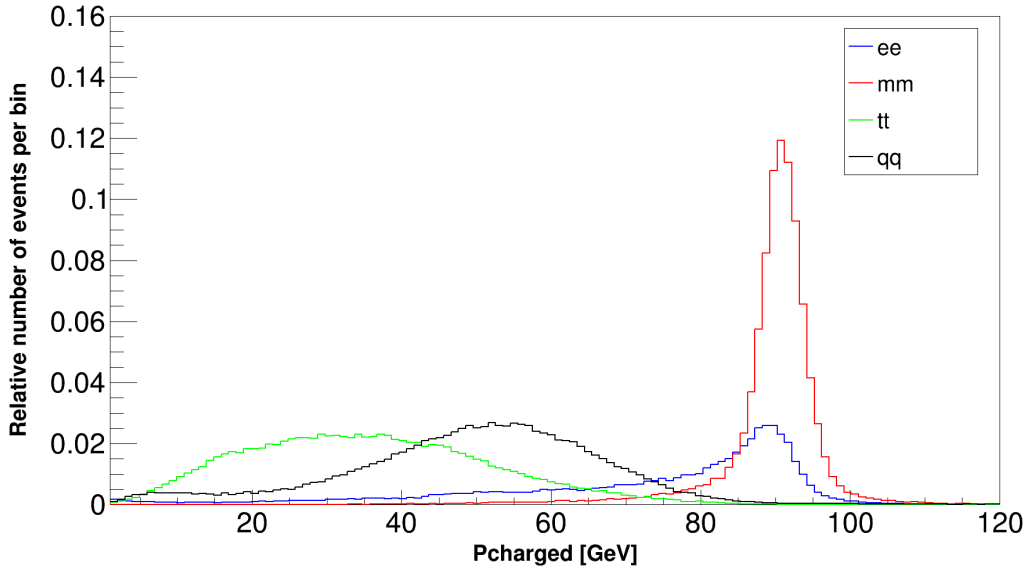


Figure 3.6: This figure shows the sum of track energies in the simulation data.

3.2.2. Cuts in P_{charged}

The separation of the data sets is less obvious in the P_{charged} channel. Most datasets overlap, making the choice harder than it was in the N_{charged} channel. However, since we have conveniently already cut against quarks in the N_{charged} channel, we can ignore said dataset and separate tauons and muons as follows:

- **Muon cut:** $P_{\text{charged}} > 71 \text{ GeV}$
- **Tauon cut:** $P_{\text{charged}} \leq 60 \text{ GeV}$

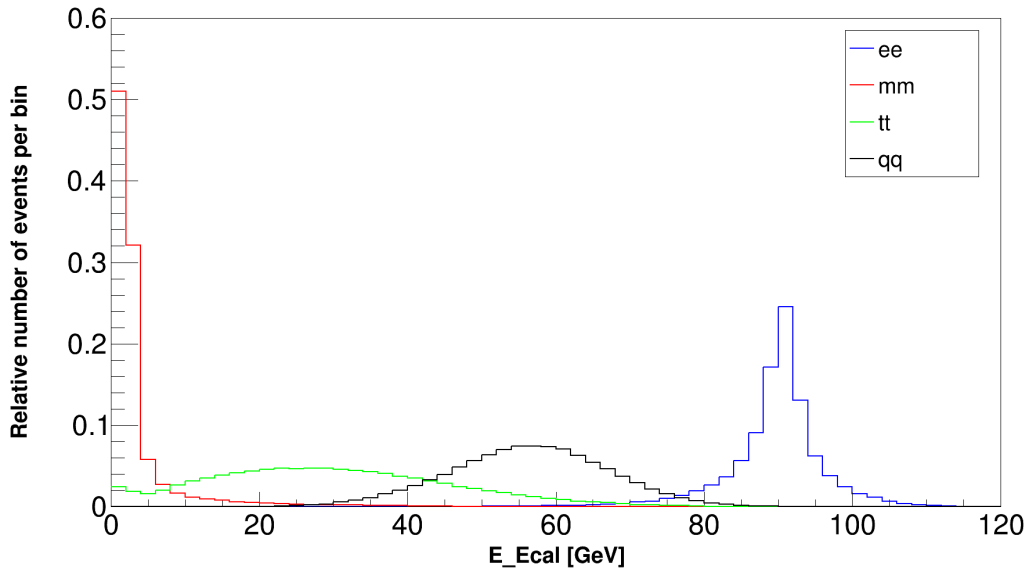


Figure 3.7: The energies deposited in the electronic calorimeter show clear differences for the four decay types and allow for effective cuts.

3.2.3. Cuts in E_{Ecal}

As has been the case for the cuts in P_{charged} , we can ignore the quark data. Instead, cuts for all leptons are applied in order to separate the three kinds:

- **Electron cut:** $E_{\text{Ecal}} \geq 70 \text{ GeV}$
- **Muon cut:** $E_{\text{Ecal}} < 50 \text{ GeV}$
- **Tauon cut:** $E_{\text{Ecal}} < 60 \text{ GeV}$

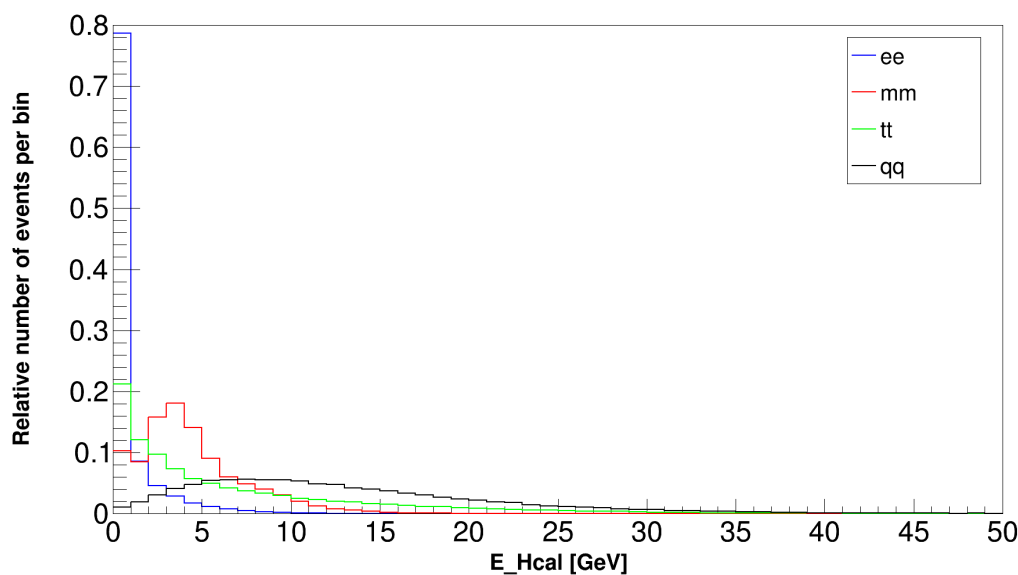


Figure 3.8: The plot shows the energies deposited in the hadronic calorimeter. The distribution of the decay types overlap significantly.

3.2.4. Cuts in E_{Hcal}

In the data from the hadronic calorimeter, the overlap between all four kinds of decay events does not allow for any kind of meaningful cuts.

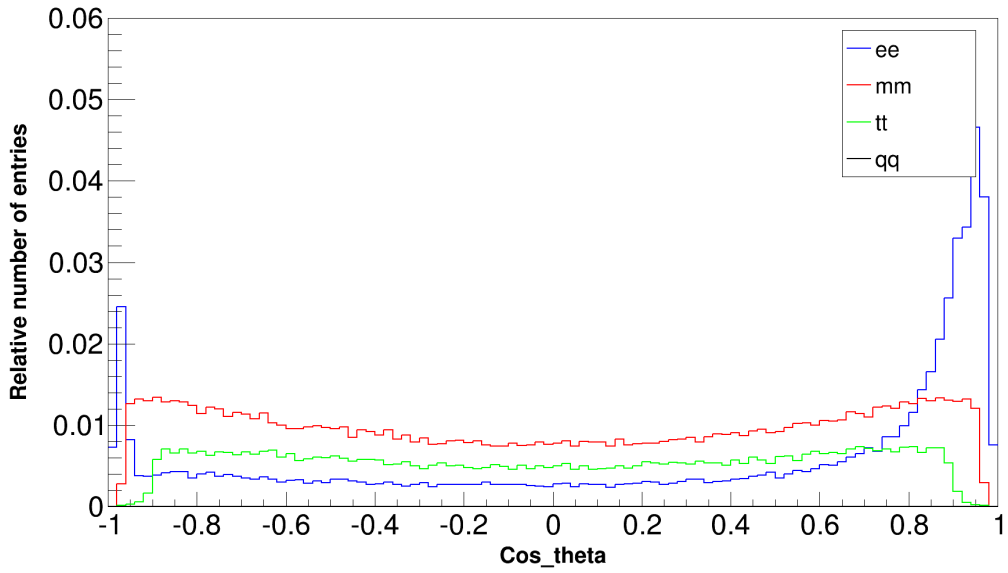


Figure 3.9: This figure shows the cosine of the angle between the beam and the direction of the created anti-lepton. Note the asymmetric peaks in the electron data, which will be discussed in the chapter on the separation of s- and t-channel.

3.2.5. Cuts in Cos_theta

As can be seen in figure 3.9, the quark events are not assigned values of Cos_theta within its natural boundaries from -1 to 1. This is due to the fact that they cause scattering jets, meaning that a well defined direction cannot be assigned. Leptonic events can also cause the creation of more than two particles. Furthermore, as there is no detection capacity in beam direction as well as for a very shallow angles, some regular events are also not assigned an angle. As a consequence, such events are listed with a Cos_theta of 999.0. Since the electron data is later divided into s- and t-channel events, for which the Cos_theta distribution is needed, it has to be ensured that the data is indeed valid. As there is no detection capacity for shallow angles to the beam direction, such events are cut off:

- **Electron cut** $-0.9 \leq \cos_{\text{theta}} \leq 0.9$

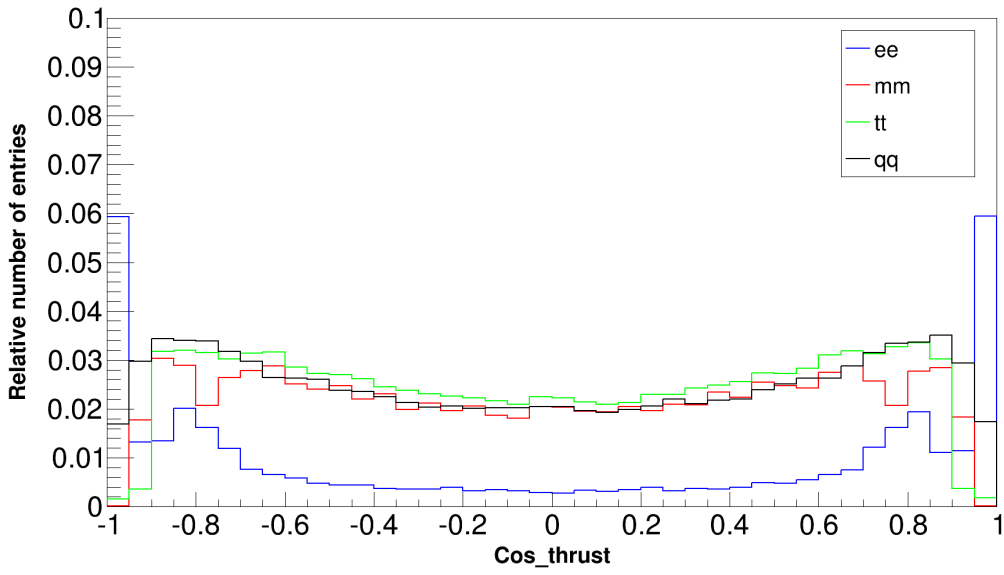


Figure 3.10: This figure shows the cosine of the angle between the beam and the thrust direction.

3.2.6. Cuts in Cos_thrust

Figure 3.10 suggests a cut to separate tauons from the rest of the particles, especially electrons, which often have have $\cos_{\text{thrust}} > 0.9$ or $\cos_{\text{thrust}} < -0.9$.

- **Tauon cut** $-0.9 \leq \cos_{\text{thrust}} \leq 0.9$

The final cuts thus are

	Ncharged	Pcharged [GeV]	E_Ecal [GeV]	Cos_theta	Cos_thrust
e^+e^-	< 7		≥ 70		$\geq -0.9 \& \leq 0.9$
$\mu^+\mu^-$	= 2	> 71	< 50		
$\tau^+\tau^-$	< 7	≤ 60	< 60		$\geq -0.9 \& \leq 0.9$
$q\bar{q}$	≥ 8				

Table 3.1: Cuts applied to separate the datasets. An additional cut on Pcharged, which is not listed here, is discussed below.

3.3. Two-photon events

One possible source of background are two-photon events. Figure 3.11 shows possible Feynman-graphs of such events. Two photons are created, without an intermediate Z^0 . As such, these measurements need to be excluded using cuts.

In the event described by the Feynman graph on the right of figure 3.11, the incident electron and proton scatter, but don't lose much energy in the process. They continue without diverging much from the beam direction. Naturally, there is no detecting capacity in beam direction, meaning these two particles are not registered. In the process of scattering, a fermion anti-fermion pair with low energy is created. They can be effectively cut by restricting $P_{\text{charged}} > 5 \text{ GeV}$ without losing much in terms of efficiency. As no charged particles are created in the event type described by the Feynman graph on the left of figure 3.11, the cut in P_{charged} also effectively cuts against these kinds of events.

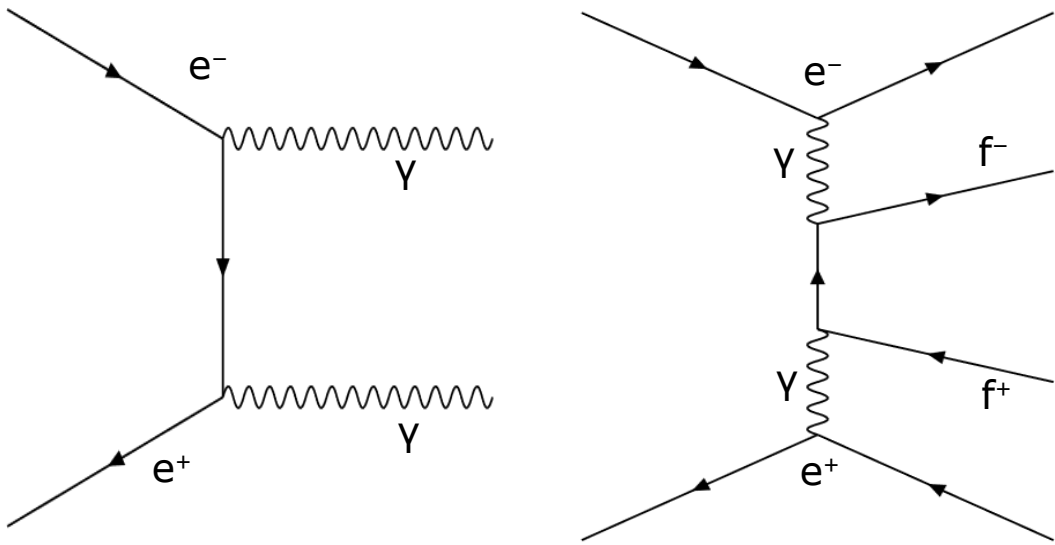


Figure 3.11: Two exemplary Feynman-graphs of two-photon events. A Z^0 is never created, which means that these event should not contribute to our measurement.

3.4. Purity and the efficiency matrix

These cuts are now applied to the simulated data, where the kind of event is known. This way, one can determine the efficiency and purity of the cuts and judge how well they work. The efficiency matrix is calculated as

$$E_{ij} = \frac{C_{ij}}{N_i}, \quad \vec{C} = \mathbf{E} \cdot \vec{N} \quad (3.1)$$

where the indexes i and j represent the kind of event. C_{ij} is thus the amount of events of type i left over after applying the cut for type j and N_i is the overall number of events

i in the simulation data.

Events	e^+e^-	$\mu^+\mu^-$	$\tau^+\tau^-$	$q\bar{q}$
Cut				
e^+e^-	0.39078	0.00002	0.00422	0.00002
$\mu^+\mu^-$	0.00018	0.90171	0.00611	0.00001
$\tau^+\tau^-$	0.00039	0.00940	0.83413	0.00094
$q\bar{q}$	0.00007	0.00001	0.00685	0.98437

Table 3.2: Efficiency matrix of the applied cuts. The diagonal elements are the self efficiencies.

As these values describe event counts, they should be distributed binomially. According to Paterno [3], the binomial error of such values is commonly calculated as

$$s_{E_{ij}} = \sqrt{\frac{E_{ij} \cdot (1 - E_{ij})}{N_i}} \quad (3.2)$$

where N_i is the number of simulated events of the appropriate kind. This yields the following matrix

Events	e^+e^-	$\mu^+\mu^-$	$\tau^+\tau^-$	$q\bar{q}$
Cut				
e^+e^-	0.001593	0.000015	0.000230	0.000014
$\mu^+\mu^-$	0.000044	0.000969	0.000277	0.000010
$\tau^+\tau^-$	0.000065	0.000314	0.001322	0.000098
$q\bar{q}$	0.000028	0.000011	0.000293	0.000395

Table 3.3: Errors of the efficiency matrix elements calculated under the assumption of binomial distribution.

To calculate the purity, it has to be taken into account that the different events do not occur with the same probability in nature, but are roughly equally represented in the simulated data. This is expressed by the branching ratio

$$BR_i = \frac{\Gamma_i}{\sum_j \Gamma_j} \quad (3.3)$$

where Γ_i is the partial decay width corresponding to event i . The partial decay widths of leptons $\Gamma_l = 83.8$ MeV and of quarks $\Gamma_q = 1732$ MeV are given in [1] without error. Using this, the purity can be calculated as

$$P_i = \frac{BR_i \cdot E_{ii}}{\sum_j BR_j \cdot E_{ij}} \quad (3.4)$$

which yields the following results:

Cut	Purity
e^+e^-	0.9882
$\mu^+\mu^-$	0.9928
$\tau^+\tau^-$	0.9661
$q\bar{q}$	0.9997

Table 3.4: Purity of the cuts. All purities are above 95%, indicating that the cuts work reasonably well.

3.5. Calculation of the inverse efficiency matrix

The efficiency matrix allows the calculation of the number of events after applying the cuts to a set of measurements where the kind of event is known:

$$\vec{C} = \mathbf{E} \cdot \vec{N} \quad (3.5)$$

where \vec{N} is a vector whose components are the numbers of events of the four different kinds and \vec{C} is a vector whose components are the number of events allocated to the four different cuts. In reality however, the kind of event is unknown and has to be determined by the cuts. Thus, the inverse of \mathbf{E} can be used to calculate the number of actual events from the known number of events after the different cuts:

$$\vec{N} = \mathbf{E}^{-1} \cdot \vec{C} =: \mathbf{I} \cdot \vec{C} \quad (3.6)$$

This means that, based on the efficiency calculations for events that are not supposed to be in the cut, a certain number of events are actually subtracted. The inverse matrix \mathbf{I} is

Events	e^+e^-	$\mu^+\mu^-$	$\tau^+\tau^-$	$q\bar{q}$
Cut				
e^+e^-	2.55899	0.00007	-0.01294	-0.00004
$\mu^+\mu^-$	-0.00051	1.10909	-0.00812	-0.00000
$\tau^+\tau^-$	-0.00120	-0.01250	1.19896	-0.00115
$q\bar{q}$	-0.00019	0.00008	-0.00835	1.01589

Table 3.5: The inverse of the efficiency matrix (table 3.2).

Since general matrix inversion cannot be expressed in an analytical formula but is done for example via the Gauss algorithm, the error calculation is not trivial. To calculate

the error of the inverse matrix, a method called *toy experiments* can be used. A normal-distributed random variable $G = \mathcal{N}(0, 1)$ is multiplied by the error of an element of the efficiency matrix and then added to said element.

$$E_{ij}^k = E_{ij} + G^k \cdot s_{E_{ij}} \quad (3.7)$$

This is done $N = 10000$ times, resulting in 10000 randomly varied efficiency matrices, which are then inverted one by one. The standard deviation of the thus calculated elements I_{ij}^k of the inverse matrices is used as the error for the inverse matrix elements I_{ij} :

$$s_{I_{ij}} = \sqrt{\frac{1}{N-1} \sum_{k=1}^N (I_{ij}^k - I_{ij})^2} \quad (3.8)$$

The resulting matrix is displayed in table 3.6

Events	e^+e^-	$\mu^+\mu^-$	$\tau^+\tau^-$	$q\bar{q}$
Cut				
e^+e^-	0.010372	0.000043	0.000703	0.000037
$\mu^+\mu^-$	0.000123	0.001187	0.000366	0.000011
$\tau^+\tau^-$	0.000196	0.000416	0.001870	0.000119
$q\bar{q}$	0.000074	0.000013	0.000353	0.000403

Table 3.6: Errors of the inverse efficiency matrix (table 3.5) calculated using the *toy experiments* method.

3.6. Separation of s- and t-channel

The electron data still includes the scattering events (t-channel), where no real Z^0 is created. The results from these measurements thus give no information about the properties of the Z^0 boson and need to be excluded from the results. In section 1.4, it was explained that these two kind of events show different angular distributions. A linear combination of said distributions, σ_s and σ_t (equation 1.11),

$$N(x) = A_s \cdot (1 + x^2) + A_t \cdot (1 - x)^{-2} \quad (3.9)$$

where A_s and A_t are fit parameters and $x = \cos_{\text{theta}}$ is the variable, was fitted to the \cos_{theta} -channel data of the events classified by the cuts as electron events. It is worth pointing out that this underground correction is done on the data itself, not on separate measurements or simulated data. The result can be seen in figure 3.12. The number of events in the s-channel N_s and t-channel N_t can then be calculated by integrating the summands respectively, with the range naturally limited by the applied cut in \cos_{theta} .

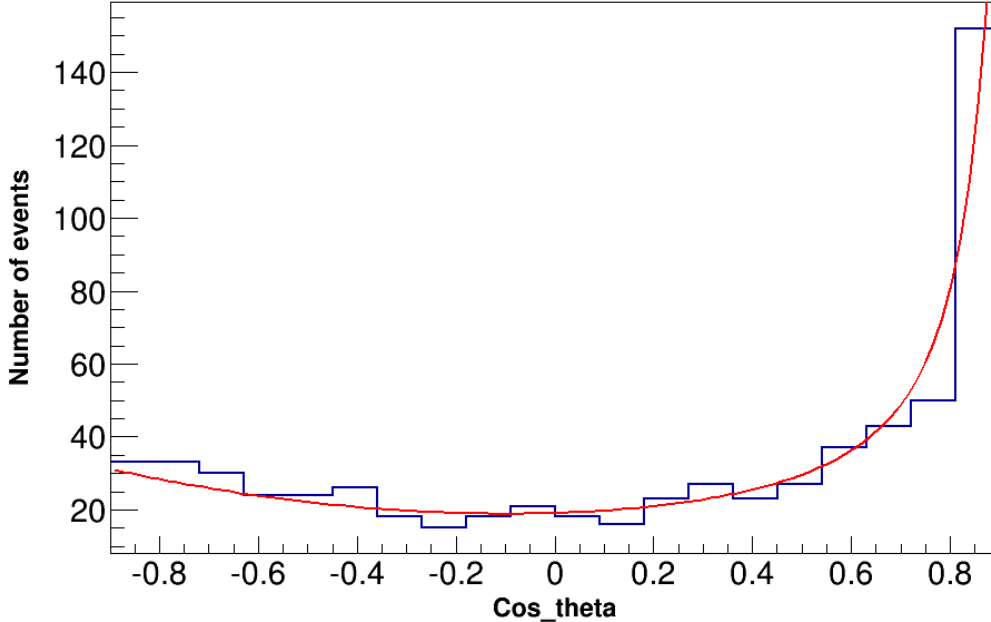


Figure 3.12: s-t channel separation for $\sqrt{s} \approx 92$ GeV. The electron cut limits \cos_{theta} to the range $-0.9 \leq \cos_{\text{theta}} \leq 0.9$.

$$N_s = A_s \cdot \int_{-0.9}^{0.9} 1 + x^2 dx =: A_s \cdot I_s, \quad N_t = A_t \cdot \int_{-0.9}^{0.9} (1 - x)^{-2} dx =: A_t \cdot I_t \quad (3.10)$$

The integrals are mere constants, $I_s \approx 2.3$ and $I_t \approx 9.5$, thus making the error calculations simpler as they might seem on first glance. The following quotient can later be used to correct the number of e^+e^- -events after the cuts

$$c_{st} = \frac{N_s}{N_s + N_t}, \quad s_{c_{st}} = \sqrt{\left(\frac{I_s \cdot N_t}{(N_s + N_t)^2} \cdot s_{A_s} \right)^2 + \left(\frac{I_t \cdot N_s}{(N_s + N_t)^2} \cdot s_{A_t} \right)^2} \quad (3.11)$$

The main issue with these calculations is the limitation imposed by the cut in \cos_{theta} . The results varied significantly when fitting over smaller ranges. For better results, the detection capacities of the detector for shallow angles would have to be examined in detail. The needed data was not provided and such measurements would surely have come in conflict with the time constraints.

3.7. Cross sections and the mass of Z^0

With the data cleared of underground effects, the cross sections can be calculated. The number of events after the respective cuts \vec{C} are Poisson-distributed, thus

$$s_{C_i} = \sqrt{C_i} \quad (3.12)$$

With equation 3.6, the error on the events \vec{N} that presumably occurred can be calculated as

$$s_{N_i} = \sqrt{\sum_{i,j} ((C_j \cdot s_{I_{ij}})^2 + (I_{ij} \cdot s_{M_j})^2)} \quad (3.13)$$

For electron-positron events, the s-t-channel separation has to be implemented:

$$N'_{e^+e^-} = c_{st} \cdot N_{e^+e^-}, \quad s_{N'_{e^+e^-}} = \sqrt{(c_{st} \cdot s_{N_{e^+e^-}})^2 + (N_{e^+e^-} \cdot s_{c_{st}})^2} \quad (3.14)$$

In order to calculate the cross sections, the radiation corrections and the luminosity of the accelerator are needed. Both were provided and are listed in the following table

\sqrt{s} [GeV]	L [1/nb]	s_L^{stat} [1/nb]	s_L^{sys} [1/nb]	s_L^{total} [1/nb]	$c_{beam,l+l^-}$ [nb]	$c_{beam,q\bar{q}}$ [nb]
88.48	675.9	3.5	4.5	5.7	0.09	2.0
89.47	543.6	3.2	3.6	4.8	0.20	4.3
90.23	419.8	2.8	2.8	4.0	0.36	7.7
91.23	3122.2	7.8	20.9	22.3	0.52	10.8
91.97	639.8	3.6	4.2	5.6	0.22	4.7
92.97	479.2	3.1	3.2	4.5	-0.01	0.2
93.72	766.8	4.0	5.1	6.5	-0.08	-1.6

Table 3.7: The luminosities L and radiation corrections c_{beam} for the different center-of-mass energies \sqrt{s} . The radiation corrections where taken from [2], where no error was given.

The cross section and their error can then be calculated as

$$\sigma_i = \frac{N_i}{L} + c_{beam,i}, \quad s_{\sigma_i} = \sqrt{\left(\frac{s_{N_i}}{L}\right)^2 + \left(\frac{N_i \cdot s_L^{total}}{L^2}\right)^2} \quad (3.15)$$

Figure 3.13 shows the result of the calculations for the muon cut (for the other graphs, see appendix). The Breit-Wigner function from equation 1.10 was changed to be

$$\sigma_f(s) = \frac{12\pi}{M_Z^2} \frac{s\Gamma_f^2}{(s - M_Z^2)^2 + s^2\Gamma_Z^2/M_Z^2} \quad (3.16)$$

where, instead of $\Gamma_e\Gamma_f$, Γ_f^2 was used for all fits, reducing the number of fit parameters. For the leptons, this means assuming lepton universality, although a small calculation using the partial decay width of the electron can be used to calculate the Γ_f without assuming universality. For the hadrons, this exact calculation is necessary and will be discussed in the next section. Above function was used for all of the following fits.

The fits yielded the following values for the mass of the Z⁰-boson

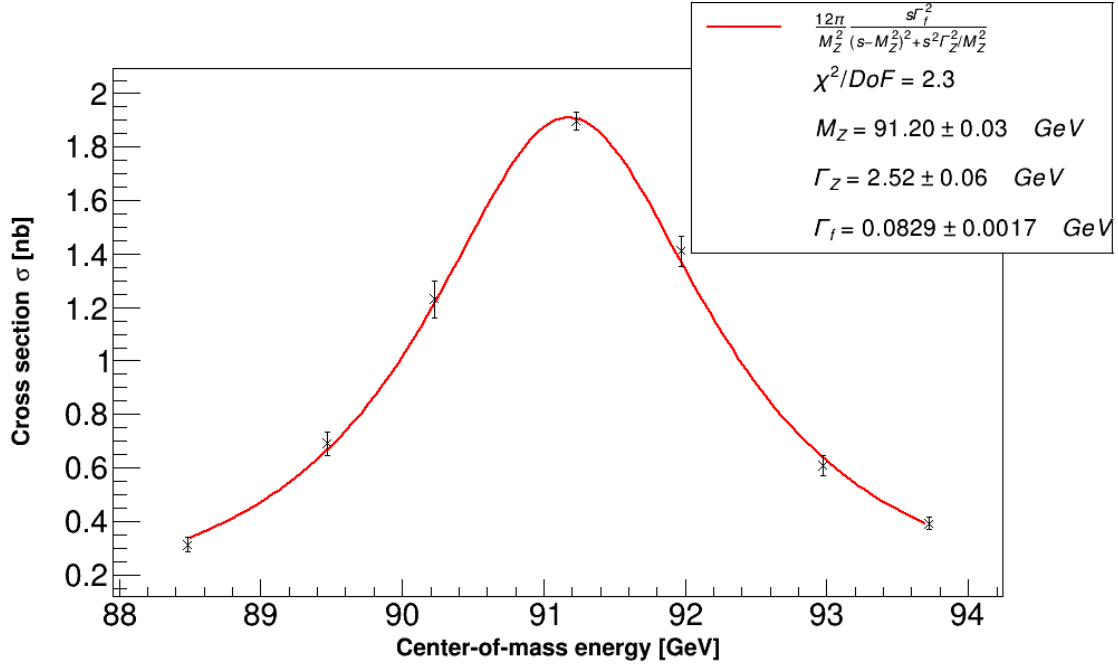


Figure 3.13: Cross sections of the different \sqrt{s} in the muon cut. The graphs for the other cuts can be found in the appendix.

Event type	M_{Z^0} [GeV]	$s_{M_{Z^0}}$ [GeV]
e^+e^-	91.11	0.06
$\mu^+\mu^-$	91.20	0.03
$\tau^+\tau^-$	91.18	0.04
$q\bar{q}$	91.189	0.009
Weighted mean	91.188	0.008
Literature value	91.187	

Table 3.8: The mass of Z^0 as it was calculated from the fits for the different cuts as well as their weighted mean. The literature value was found in [4] (no error listed).

The weighted mean is in very good agreement with the literature value, enclosing it in its relatively small ($<0.01\%$) 1σ interval.

3.8. Decay widths and the neutrino generations

The Breit-Wigner fits also included the decay widths as fit parameters. The results are listed in table 3.9.

Event i	Γ_Z [GeV]	s_{Γ_Z} [GeV]	Γ_i [MeV]	s_{Γ_i} [MeV]	Γ_i^{lit} [MeV]	Γ_i^{calc} [MeV]
e^+e^-	2.28	0.11	94	4	83.8	83.4
$\mu^+\mu^-$	2.52	0.06	82.9	1.7	83.8	83.4
$\tau^+\tau^-$	2.48	0.07	76.9	1.9	83.8	83.4
$q\bar{q}$	2.526	0.019	1777	41	1732	1742

Table 3.9: The decay widths resulting from the Breit-Wigner fits and their literature value (from [1], no error given) for comparison. The values that were theoretically calculated by the authors during the preparation for the experiment are listed in the last column.

The partial decay width Γ_q of the quark events was calculated from the fit parameter Γ_f^q as

$$\Gamma_q = \frac{(\Gamma_f^q)^2}{\Gamma_e}, \quad s_{\Gamma_q} = \sqrt{\left(\frac{2\Gamma_f^q}{\Gamma_e} \cdot s_{\Gamma_f^q} \right)^2 + \left(\frac{(\Gamma_f^q)^2}{\Gamma_e^2} \cdot s_{\Gamma_e} \right)^2} \quad (3.17)$$

where the results from the muon fits were used for the partial decay width of the electron Γ_e . This can be done since we have already assumed lepton universality and is reasonable, because the electron results include the s-t-channel separation, which, as discussed, is a significant source of error. Furthermore, the purity (table 3.4), was the highest for muon cuts, while the efficiency was still the best for among the lepton cuts. See table B.1 in the appendix for the results not assuming universality.

The tauon events are a less reliable source due to their comparatively complex signature (see figure 3.3). As a result, the simulated tauon data showed significant overlaps with the other data sets in all analysis channels, thus making it difficult to define efficient cuts with high purity. Incidentally, the muon events are also the only lepton event that includes the literature and theoretical values in their 1σ interval. The result for the electron events is higher than expected and includes said values only in its 3σ interval. This is likely due to the s-t-channel separation. If not all Bhabha scattering events are excluded, the cross section increases, and with it the decay width resulting from the fits. More data could improve the fit that was done to the \cos_{theta} distribution of the electron cuts.

To calculate the amount of neutrino generations $n_{\nu\text{-gen}}$, one first has to calculate the blind decay width

$$\Gamma_{blind} = \Gamma_Z^{ave} - 3 \cdot \Gamma_l - \Gamma_{q\bar{q}} = (0.49 \pm 0.04) \text{ GeV} \quad (3.18)$$

where $\Gamma_Z^{ave} = (2.516 \pm 0.017) \text{ GeV}$ is the weighted average of the four calculated Γ_Z . Again assuming lepton universality, the muon result was used for Γ_l . The blind decay width is then divided by the theoretically calculated decay width $\Gamma_{\nu}^{calc} = 0.1676 \text{ GeV}$

(see table A.1) of a single neutrino generation.

$$n_{\nu\text{-}gen} = \frac{\Gamma_{\nu}^{\text{blind}}}{\Gamma_{\nu}^{\text{calc}}} = (2.93 \pm 0.26) \quad (3.19)$$

Even the 3σ interval encloses no other integers than 3, meaning that it can be said with quite some confidence that there are 3 neutrino generations.

3.9. Forward-backward asymmetry

The forward ($0 < \cos_{\text{theta}} < 1$) and backward ($-1 < \cos_{\text{theta}} < 0$) events were counted for the second, forth and sixth center-of-mass energy, $\sqrt{s} \approx 89.5, 91.23$ and 93.0 GeV. This represents the integrals in equation 1.12, as the cross sections are proportional to the number of events. The asymmetry can then be calculated as

$$A_{fb} = \frac{N_f - N_b}{N_f + N_b}, \quad s_{A_{fb}} = 2\sqrt{\frac{N_f^2 s_{N_f}^2 + N_b^2 s_{N_b}^2}{(N_f + N_b)^4}} = 2\sqrt{\frac{N_f N_b}{(N_f + N_b)^3}} \quad (3.20)$$

where N_f and N_b are the event counts, $s_{N_f} = \sqrt{N_f}$ and $s_{N_b} = \sqrt{N_b}$ are their binomial errors, thus justifying the simplification in above equation. Equation 1.14 now allows the calculation of the Weinberg angle. For that it has to be solved for the angle

$$\theta_w = \arcsin\left(\sqrt{\frac{1 - \sqrt{A_{fb}/3}}{4}}\right), \quad s_{\theta_w} = \frac{1}{4}\sqrt{-\frac{s_{A_{fb}}^2}{A_{fb}(\sqrt{12A_{fb}} + A_{fb} - 9)}} \quad (3.21)$$

As this formula only holds for the center of the resonance peak, no angles could be calculated even though positive asymmetries were calculated for off-peak center-of-mass. Inserting the value $\theta_w = 28.7^\circ$ [5] in equation 1.14 yields an expected asymmetry of $A_{bf}^{\text{lit}} \approx 0.018$.

As the asymmetry is negative for $\sqrt{s} \approx 91.23$ GeV, the calculated Weinberg angle

\sqrt{s} [GeV]	N_f	N_b	A_{fb}	$s_{A_{fb}}$	θ_w [°]	s_{θ_w} [°]
89.5	117	112	0.02	0.07	-	-
91.23	1845	1881	-0.010	0.016		
93.0	153	99	0.21	0.06	-	-

Table 3.10: The Weinberg angle for calculated for three different center-of-mass energies. The Weinberg angle can be found in [4] as $\theta_w^{\text{lit}} = 28.7426^\circ$. Calculations for $\sqrt{s} \approx 91.23$ GeV yielded complex angles.

is complex. The 1σ interval around the asymmetry includes positive values and the 2σ interval includes the expected value for the asymmetry. In fact, all values for the asymmetry include the expected value, but their errors margins, in particular that for

$\sqrt{s} \approx 89.5$ GeV being $> 300\%$, are very wide. This stems from the low number of counts and the fact that a difference of two values with a large relative error is calculated. More data would greatly increase the accuracy and allow for more reliable results for the asymmetry.

According to [4], the Weinberg angle itself can also be calculated as from the mass of the Z^0 -boson and some constants.

$$\theta_w = \arcsin \left(\sqrt{\frac{1}{2} - \sqrt{\frac{1}{4} - \frac{\pi \cdot \alpha(M_Z^2)}{\sqrt{2} \cdot G_F \cdot M_Z^2}}} \right) \quad (3.22)$$

$$s_{\theta_w} = \sqrt{\frac{\pi}{4\sqrt{2}}} \cdot \sqrt{\frac{s_{M_Z}^2 \cdot \alpha(M_Z^2)}{M_Z^2 \cdot (G_F M_Z - 2\sqrt{2}\pi\alpha(M_Z^2))}}$$

Converted to degrees, the results it $\theta_w = (28.746 \pm 0.004)^\circ$, which encloses the literature value $\theta_w^{lit} = 28.7426^\circ$ [4] in its 1σ interval. This had to be expected given the precision and accuracy of the mass measurement. However, this calculation uses constants that are not easy to determine experimentally and thus only has little meaning for the results obtained in these measurements.

4. Conclusion

The mass of the Z^0 boson could be determined with high accuracy

$$M_Z = (91.188 \pm 0.008) \text{ GeV}$$

and matches the literature value $M_z^{lit} = 91.187 \text{ GeV}$ [4] within its 1σ interval. The total decay width Γ_Z of the Z^0 decay channel was calculated as

$$\Gamma_Z = (2.516 \pm 0.017) \text{ GeV}$$

which includes $\Gamma_Z^{lit} = (2.4952 \pm 0.0023) \text{ GeV}$ [6] in its 2σ margin. The error in the decay width largely originates from the efficiency matrix, which was calculated using the simulated data. The simulations were done at $\sqrt{s} \approx 91.3 \text{ GeV}$, which is roughly the resonance energy of the Z^0 decay. The actual efficiencies of the applied cuts might vary for the off-resonance data points, thus causing the discrepancy in the decay widths. Perhaps for the same reason, the expected results assuming lepton universality could not be reproduced. The partial decay widths of the lepton events calculated by the authors were

$$\Gamma_{e^+e^-} = (94 \pm 4) \text{ MeV}$$

$$\Gamma_{\mu^+\mu^-} = (82.9 \pm 1.7) \text{ MeV}$$

$$\Gamma_{\tau^+\tau^-} = (76.9 \pm 1.9) \text{ MeV}$$

These results only match within multiples of their σ intervals, meaning that the results neither confirm nor obviate lepton universality. The muon result was the only to include the expected lepton decay width of $\Gamma_l^{lit} = 83.8 \text{ MeV}$ [1] and was used to calculate the quark decay width from the fit results as $\Gamma_{q\bar{q}} = (1777 \pm 41) \text{ MeV}$. The literature value $\Gamma_{q\bar{q}}^{lit} = 1732 \text{ MeV}$ is slightly outside the 1σ interval.

Using these results, the number of neutrino generations was estimated from the blind decay width $\Gamma_{blind} = (0.49 \pm 0.04) \text{ GeV}$ to be $n_\nu = (2.93 \pm 0.26)$. This leaves all integers but 3 outside of the 3σ margin, thus solidly confirming the number of neutrino generations predicted by the Standard Model.

5. References

- [1] *Analyse von Z^0 Zerfällen.* Albert-Ludwig University of Freiburg, Freiburg, Feb. 9 1995.
- [2] *Anleitung des Versuches "Z⁰-Resonanz".*, Albert-Ludwig University of Freiburg, Freiburg, Mar. 2 2012.
- [3] Paterno, Marc. "Calculating efficiencies and their uncertainties." FNAL/CD/CEPA/SLD, May 5, 2003. Access date: <http://home.fnal.gov/paterno/images/effic.pdf> (April 21 2016 13:00.)
- [4] *Analyse von Z^0 Zerfällen.* Ludwig-Maximilian University of Munich, Munich, Oct. 14 2010.
- [5] Griffiths, David. *Einführung in die Elementarteilchenphysik.* Berlin: Akademischer Verlag, 1996 (Orig.: "Introduction to Elementary Particles". New York 1987.)
- [6] Jakobs, Karl. *Experimentalphysik V - 11. Experimentelle Tests der elektroschwachen Wechselwirkung.*
<https://portal.uni-freiburg.de/jakobs/dateien/vorlesungsdateien/ex5-14/kap11>
(22.04.2016)
- [7] Universität Zürich. *Standard Model.*
<http://www.physik.uzh.ch/groups/serra/StandardModel.html> (23.04.2016)
- [8] K.A. Olive et al. (Particle Data Group), Chin. Phys. C, 38, 090001 (2014) and 2015 update
- [9] The OPAL Experiment at LEP 1989-2000.
<http://opal.web.cern.ch/Opal> (23.04.2016)

A. Calculation of decay widths and cross sections at resonance

A.1. Decay widths

The decay width for the decay of a Z^0 boson into a fermion f is given by [4]:

$$\Gamma_f = \frac{N_c^f \cdot \sqrt{2}}{12\pi} \cdot G_F \cdot M_Z^3 \cdot (g_V^{f2} + g_A^{f2}) \quad (\text{A.1})$$

with the color factor N_c^f , the Fermi constant G_F , the Z^0 mass M_Z , the electric charge Q_f , the vector coupling strength g_V^f and the axial vector coupling strength g_A^f . Using equation 1.5, one can obtain:

$$\Gamma_f = \frac{N_c^f \cdot \sqrt{2}}{12\pi} \cdot G_F \cdot M_Z^3 \cdot \left(\left(I_3^f - 2Q_f \sin^2(\theta_w) \right)^2 + I_3^{f2} \right) \quad (\text{A.2})$$

The Fermi constant and the Z^0 mass are [4]

$$\begin{aligned} G_F &= 1.16639 \cdot 10^{-5} \text{ GeV}^{-2} \\ M_Z &= 91.187 \text{ GeV} \end{aligned} \quad (\text{A.3})$$

and for the Weinberg angle the following relation is used [5]:

$$\sin^2(\theta_w) = 0.23 \quad (\text{A.4})$$

The other parameters depend on which fermion is produced:

$$N_c^f = \begin{cases} 1 & \text{if } f = \nu, e, \mu, \tau \\ 3(1 + \delta_{QCD}) & \text{if } f = u, d, s, c, b \end{cases} \quad (\text{A.5})$$

$\delta_{QCD} = 1.05 \frac{\alpha_S(M_Z)}{\pi}$ is a correction factor to account for higher order processes of the strong interaction (s. section 1.5), where $\alpha_S(M_Z) = 1/128.87$ is the strong coupling constant.

The third component of the weak isospin is:

$$I_3^f = \begin{cases} 1/2 & \text{if } f = \nu, u, c \\ -1/2 & \text{if } f = e^-, \mu^-, \tau^-, d, s, b \end{cases} \quad (\text{A.6})$$

And the electric charge:

$$Q_f = \begin{cases} 0 & \text{if } f = \nu \\ -1 & \text{if } f = e^-, \mu^-, \tau^- \\ 2/3 & \text{if } f = u, c \\ -1/3 & \text{if } f = d, s, b \end{cases} \quad (\text{A.7})$$

Plugging those values in equation A.2 yields table A.1:

	$\Gamma_{\text{rech}}/\text{MeV}$	$\Gamma_{\text{lit}}/\text{MeV}$
e, μ,τ	83.4106	83.8
ν_e,ν_μ,ν_τ	165.881	167.6
u,c	296.868	299
d,s,b	382.646	378

Table A.1: Table of partial decay widths for different fermions, calculated and literature value[4]

To get partial decay width for the decay to any charged lepton, one must simply sum up the decay width of the charged leptons. The hadronic, the neutral leptonic and the total decay width can be calculated similarly (s. table A.2).

	$\Gamma_{\text{rech}}/\text{MeV}$	$\Gamma_{\text{lit}}/\text{MeV}$
$\Gamma_e + \Gamma_\mu + \Gamma_\tau$	250.232	251.4
$3 \cdot \Gamma_\nu$	497.643	502.8
$\sum_q \Gamma_q$	1741.67	1732
total	2489.55	2486.2

Table A.2: Summarized decay width: charge leptonic, neutral leptonic and hadronic

If another lepton family exists, one expects the total decay width to increase by:

$$\frac{\Gamma_e + \Gamma_{\nu_e}}{\Gamma_{\text{total}}} = 10.0\% \quad (\text{A.8})$$

A.2. Cross sections at resonance peak

With the values calculated above, the expected cross section at the resonance peak ($\sqrt{s} = M_Z$) can be calculated with equation 1.10. The results can be seen in table A.3

	$\sigma_{peak} [nb]$
e, μ,τ	2.00524
ν_e, ν_μ, ν_τ	4.01047
u,c	7.15472
d,s,b	9.0451
$e + \mu + \tau$	6.01571
$\nu_e + \nu_\mu + \nu_\tau$	12.0314
hardronic	41.4447
total	59.4871

Table A.3: Cross sections for the $e^+e^- \rightarrow f\bar{f}$ reaction at center-of-mass energies equal to the mass of Z^0 .

B. Figures

B.1. Cross section fit graphs

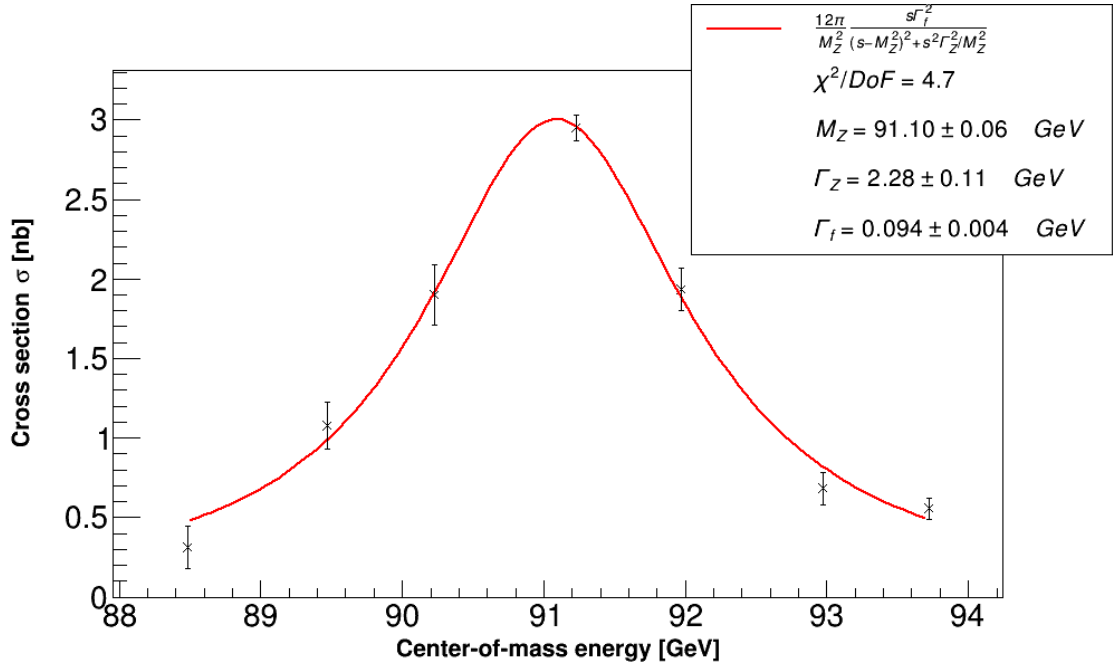
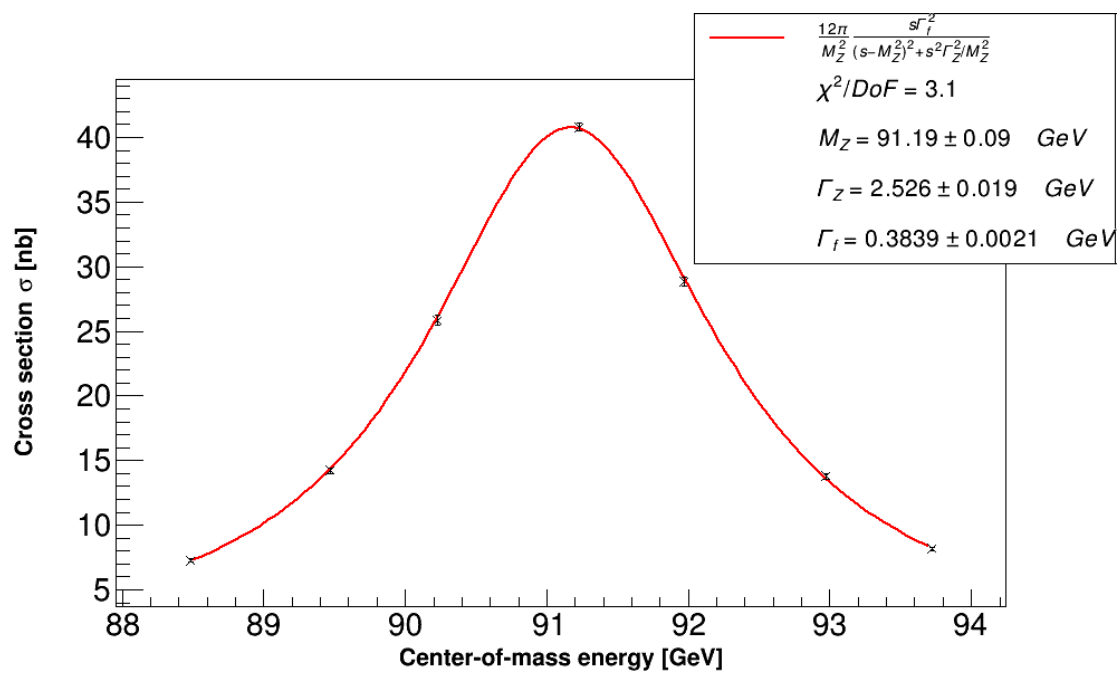
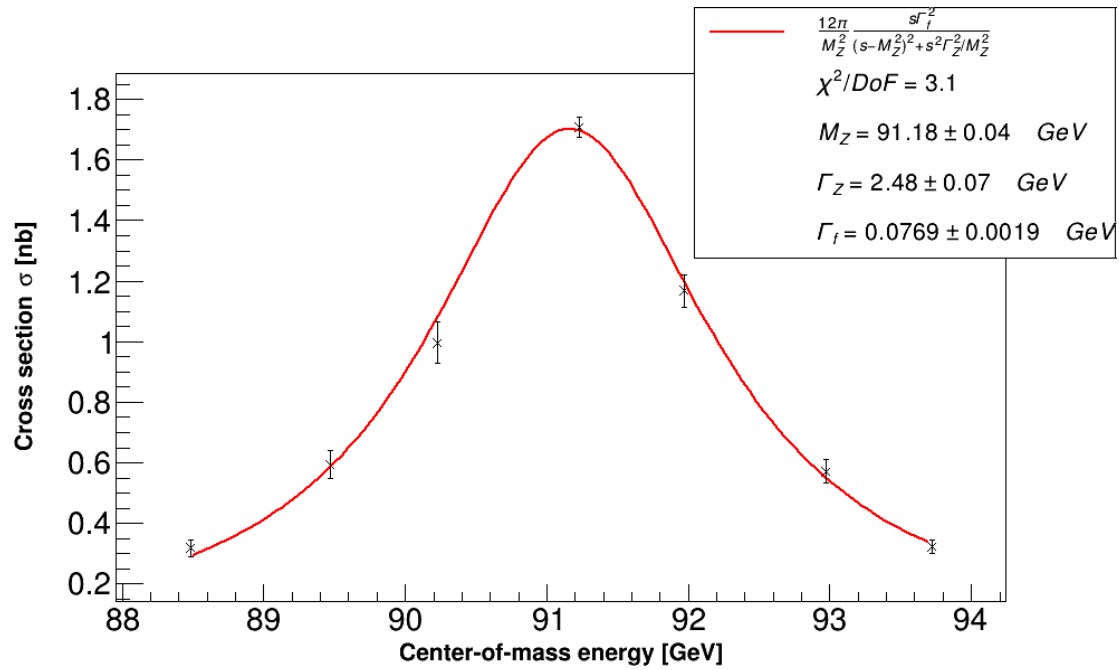


Figure B.1: Cross sections of the different \sqrt{s} in the electron cut.



To not assume lepton universality, the values can be calculated from the fit parameters as follows

$$\Gamma_i = \frac{\Gamma_f^2}{\Gamma_e}$$

Event i	Γ_Z [GeV]	s_{Γ_Z} [GeV]	Γ_i [MeV]	s_{Γ_i} [MeV]	Γ_i^{lit} [MeV]
e^+e^-	2.28	0.11	94	4	83.8
$\mu^+\mu^-$	2.52	0.06	73	4	83.8
$\tau^+\tau^-$	2.48	0.07	63	4	83.8
$q\bar{q}$	2.526	0.019	1570	70	1732

Table B.1: The decay widths when not assuming universality. Clearly, the results are much worse.